








Solar Prominence Bubble and Plumes Caused By an Eruptive Magnetic Flux Rope

Changxue Chen^{1,2} , Yang Su^{1,2} , Jianchao Xue¹ , Weiqun Gan¹ , and Yu Huang¹ 

¹ Key Laboratory of Dark Matter and Space Astronomy, Purple Mountain Observatory, Chinese Academy of Sciences, Nanjing 210023, People's Republic of China; yang.su@pmo.ac.cn, xuejc@pmo.ac.cn

² School of Astronomy and Space Science, University of Science and Technology of China, Hefei 230026, People's Republic of China
Received 2021 October 16; revised 2021 November 18; accepted 2021 November 19; published 2021 December 9

Abstract

Prominence bubbles and plumes often form near the lower prominence–corona boundary. They are believed to play an important role in mass supply and evolution of solar prominences. However, how they form is still an open question. In this Letter we present a unique high-resolution $H\alpha$ observation of a quiescent prominence by the New Vacuum Solar Telescope. Two noteworthy bubble–plume events are studied in detail. The two events are almost identical, except that an erupting mini filament appeared below the prominence–bubble interface in the second event, unlike the first one or any of the reported bubble observations. Analysis of the $H\alpha$ and extreme-ultraviolet data indicates that the rising magnetic flux rope (MFR) in the mini filament is the cause of bubble expansion and that the interaction between the prominence and MFR results in plume formation. These observations provided clear evidence that emerging MFR may be a common trigger of bubbles and suggested a new mechanism of plumes in addition to Rayleigh–Taylor instability and reconnection.

Unified Astronomy Thesaurus concepts: [Solar prominences \(1519\)](#); [Quiescent solar prominence \(1321\)](#); [Solar filaments \(1495\)](#); [Solar filament eruptions \(1981\)](#)

Supporting material: animations

1. Introduction

Prominences are dense and cold plasma structures commonly seen in hot corona whose eruption can produce flares and coronal mass ejections (Lawrence 2015). Prominence bubbles are semicircular “voids” often found underneath prominences. Upward plumes usually form at the boundaries between bubbles and prominences and emerge into the prominence body (Berger et al. 2010, 2017). Prominence bubbles and plumes play an important role in the mass supply and evolution of prominences (Berger et al. 2011). Although it has long been believed that their growth is closely related to Rayleigh–Taylor (Berger et al. 2010; Hillier et al. 2011) or coupled Kelvin–Helmholtz Rayleigh–Taylor instabilities (Berger et al. 2017; Awasthi & Liu 2019), how they form is still an open question.

Over the past decade, the formation of prominence bubbles is generally believed to be related to the emergence of magnetic flux below the prominence (Berger et al. 2011; Dudík et al. 2012; Gunár et al. 2014; Shen et al. 2015), but so far, no direct observation evidence has been found because almost all prominence bubbles are observed at the solar limb, resulting in a lack of photospheric magnetic field observations. Recently, the investigation of on-disk bubbles has revealed the magnetic topology inside bubbles where a set of magnetic loops is rooted on a magnetic patch (Guo et al. 2021). However, this research cannot solve the key question due to the lack of vital observations of the bubble formation process.

In this Letter, we present a detailed study of two bubble–plume events and show the important role of eruptive MFR. An overview of the observation and data processing is described in Section 2. In Section 3 we describe the common features

observed in both events. The detailed and unique process in the second event is shown in Section 4. Conclusions and discussions can be found in Section 5.

2. Observation Overview and Data Processing

A high-latitude quiescent prominence was observed above the northeast solar limb (42° N, 90° E) on 14 April 2021 by the New Vacuum Solar Telescope (NVST, Liu et al. 2014; Yan et al. 2020) at $H\alpha$ line center 6562.8 \AA and two offbands $\pm 0.4 \text{ \AA}$. The high-spatial-resolution images ($\sim 0''.165$ per pixel) revealed the dynamic evolution of prominence bubble and plumes. Simultaneously, the Atmospheric Imaging Assembly (AIA, Lemen et al. 2012) instrument on board the Solar Dynamics Observatory (SDO, Pesnell et al. 2012) provided full-disk EUV images with a pixel size of $0''.6$ and a cadence of 12 s.

The NVST $H\alpha$ center maps are sampled to co-align with AIA 171 \AA maps by matching specific features. Other $H\alpha$ center maps are co-aligned with each other based on cross correlation and a modified moment algorithm (Yang et al. 2015; Feng et al. 2012). This method first calculated the pixel-level displacements between reference image and target image by calculating Fourier cross correlation and then determining the subpixel displacements by applying a modified moment method to measure the centroid of the peak in the cross correlation surface. The $H\alpha$ off-band maps are co-aligned with $H\alpha$ center maps manually.

In order to derive Doppler velocity from NVST $H\alpha$ observations, a 3-points measurement method is adopted, which is described in detail by Xue et al. (2021). Assuming that the off-disk $H\alpha$ line is optically thin and the continuum is negligible (Gouttebroze et al. 1993), the off-disk $H\alpha$ lines

roughly have Gaussian profiles

$$I = I_0 \exp \left[- \left(\frac{\lambda - \lambda_D}{w} \right)^2 \right], \quad (1)$$

where I is the intensity at wavelength λ , I_0 is the observational central intensity, λ_D is the central wavelength and w is the Gaussian width of the profile. After subtracting the stray light measured beyond the prominence, we take wavelengths $\lambda_1 - \lambda_3$ ($-0.4, 0, 0.4 \text{ \AA}$) and corresponding intensities $I_1 - I_3$ into Equation (1), three main line parameters can be obtained as

$$\begin{cases} \lambda_D = \frac{1}{2} \frac{\lambda_1^2 \ln \frac{I_3}{I_2} + \lambda_2^2 \ln \frac{I_1}{I_3} + \lambda_3^2 \ln \frac{I_2}{I_1}}{\lambda_1 \ln \frac{I_3}{I_2} + \lambda_2 \ln \frac{I_1}{I_3} + \lambda_3 \ln \frac{I_2}{I_1}}, \\ w^2 = \frac{\lambda_1^2 + 2(\lambda_2 - \lambda_1)\lambda_D - \lambda_2^2}{\ln \frac{I_2}{I_1}}, \\ I_0 = I_1 \exp \left[\left(\frac{\lambda_1 - \lambda_D}{w} \right)^2 \right]. \end{cases} \quad (2)$$

With the λ_D modified by a Doppler shift, the Doppler speed v_D can be derived from

$$v_D = c \frac{\lambda_D}{\lambda_0}, \quad (3)$$

where c is the light speed and $\lambda_0 = 6562.8 \text{ \AA}$ is the $H\alpha$ rest wavelength. Nonthermal velocity can be derived from w . To satisfy the assumption of optically thin emission, we perform the calculation of spectral parameters on bright $H\alpha$ structures above 7 Mm from the solar limb. More detailed analyses of the limitations of this method and its comparison with a normal Gaussian fitting method can be found in Xue et al. (2021).

3. The Common Features

The prominence is a hedgerow type, which consists of long and vertical threads (Figure 1). A distinct bubble is located at the base of the right part of the prominence and appears as a dark semicircular dynamic void in the $H\alpha$ images, while in the AIA EUV images, it is bright relative to the dark prominence, indicating strong, optically thin emission. The first bubble–plume event occurred between 06:19 and 06:50 UT (referred as Event A), and the second event occurred between 07:50 and 08:20 UT (referred as Event B). Detailed evolution of the two events is displayed in Figure 2.

We can visually see the rising plumes in the series of NVST $H\alpha$ and AIA 193 \AA images (see Figure 2 and Movie 1). In order to show their motion characteristics, we construct time–distance diagrams by taking slices off the original images along the trajectory of the plumes (S1 in Event A and S2 in Event B, see Figure 1) and stacking them up chronologically. All slices are 2 pixels wide. We estimate the average rising speed by linearly fit the time–distance profile of corresponding upward structures.

In AIA 193 \AA channel, time–distance diagrams have higher time resolution and have no data gap. We draw diamonds and plus signs with an edge detection approach using the IDL procedure `canny.pro` to show detailed and continuous displacement of the upper boundary of the bubbles, plumes, and mini filament (Figures 3 and 4).

The evolution of the bubble and plumes we studied here is consistent with that of previous observations. In both events, it took the bubble several minutes to inflate into a semicircle void before plume initiation, which was consistent with previous observations (Berger et al. 2010; Xue et al. 2021). At the same time, the interface between the bubble and prominence showed a brightness enhancement in $H\alpha$ images (Figure 2). Such enhancement has been reported and studied in detail (Xue et al. 2021). The average rising speed of the bubble–prominence interface in the plane of the sky was 4.4 km s^{-1} in Event A (Figure 3) and 5.2 km s^{-1} in Event B (Figure 4).

The formation of the plume began with the bulge at the top of the semicircular bubble, then the plume kept rising and gradually separated from the bubble, with an average ascent speed of 16.5 km s^{-1} in Event A and 13.8 km s^{-1} in Event B, eventually splitting into many small voids before fading into the prominence (see movie 1). The rising speeds of bubble and plumes are both close to the typical values of $12\text{--}30 \text{ km s}^{-1}$ (de Toma et al. 2008; Berger et al. 2010).

During the evolution of the plume in Event A, short finger-shaped structures (hereinafter referred to as fingers) occurred first at the front and spread to the whole plume boundary as the plume gradually separated from the bubble (Figure 2). These fingers have been frequently reported in observations (Berger et al. 2008; Awasthi & Liu 2019) and predicted in magneto-hydrodynamic (MHD) simulations of Rayleigh–Taylor instability (Hillier et al. 2012; Keppens et al. 2015; Xia & Keppens 2016).

Significant brightening enhancement was observed in the bubbles after plume formation in both events (AIA 193- \AA images in Figure 2), indicating energy release may occur here. Similar brightening has been reported before (Shen et al. 2015) and was considered to be closely related to the collapse and oscillation of the bubble boundary in that event.

4. Bubble–plume Event B

What makes the observation special is the erupting looplike structure visible in the bubble around 07:59 (Figures 2(c) and (d)) in the second event. The fact that the structure is bright in $H\alpha$ images and dark in EUV images indicates its low temperature ($7\text{--}10 \times 10^3 \text{ K}$), resembling a mini filament. The line of sight (LOS) velocity map (Figure 4(c)) derived from the three-band NVST $H\alpha$ images shows that the structure is blueshifted in the upper part and redshifted in the lower part, suggesting plasma flows along a helical structure (Li et al. 2014). These facts indicate that the structure is a magnetic flux rope in an erupting mini filament.

The mini filament appeared above the limb around 07:52 and rose at an average speed of 9.7 km s^{-1} (Figure 4). At the same time, the bubble–prominence interface started to rise at a slower speed of $\sim 5.2 \text{ km s}^{-1}$. The mini filament faded as it rose and expanded and disappeared in both $H\alpha$ and EUV shortly before contact with the interface around 08:02. Then the bubble began to collapse and the upper part of the boundary arched up to form a plume with fingers.

According to these observations, we propose that the mini filament does ascend into the bubble–prominence interior rather than the result from the coincidental alignment of the mini filament and the prominence along LOS. We come to this conclusion based on the following facts. (1) The bubble begins to inflate at the same time when the mini filament appears and rises. In addition, the movement trend of the mini filament and

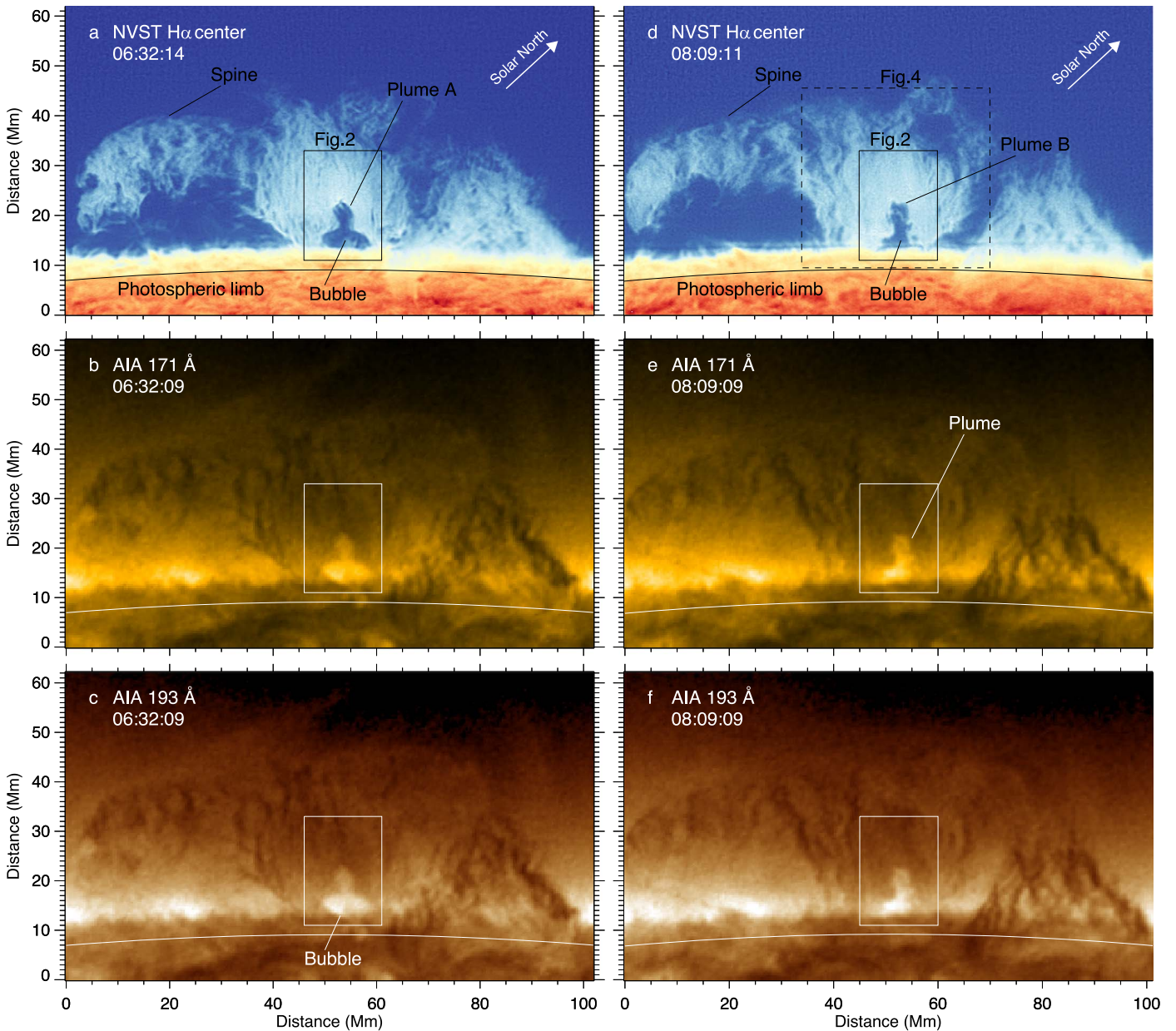


Figure 1. Quiescent prominence observed on the northeast solar limb on 2021 April 14. Left: multi-wavelength observations of the bubble–plume Event A. Right: observations of the bubble–plume Event B. From top to bottom: images taken at $H\alpha$, AIA 171 Å, and AIA 193 Å, respectively. In the AIA EUV images, the bubbles and plumes show optically thin emission relative to a surrounding dark prominence due to significant continuum absorption. All images have the photospheric limb (marked with black or white curves) rotated to be horizontal, and the solar north are marked with arrows in (a) and (d). The bubbles located at the base of the right part of the prominence are noted as are the large rising plumes. The black or white boxes outline the field of view (FOV) of the images in Figure 2 for Event A (left panels) and Event B (right panels), respectively. The dashed box in panel (d) outlines the FOV of the Doppler maps in Figures 4(c) and (d). An animation of the events’ evolution is provided. Event A runs from about 05:59 UT to after 07:03:33 UT while Event B begins at approximately 7:27 UT and ends after 08:31 UT. The real-time duration of the animation is 7 s.

(An animation of this figure is available.)

bubble–prominence interface is also consistent. (2) The mini filament disappears before it reaches the bubble–prominence interface rather than continuing to rise or expand. Meanwhile, the bubble boundary is clearly brightened and disturbed. (3) The Doppler shift of the main body of the prominence has no significant change, except that after the mini filament disappears at the interface, the top part of the interface changes from strong redshift to blueshift (Figure 4(d)). All these clues indicate that the expansion of the bubble, the turbulence at the boundary of the bubble, and the plume initiation are closely related to the eruption of the mini filament.

Our results present an excellent perspective of bubble formation in which the bubble evolves from a small and flat void into a semicircular void as the mini filament rises and expands inside it, which proves that bubble formation is connected to emerging magnetic flux.

Moreover, the erupting MFR is also the cause of the plumes. This is different from the idea that is widely accepted, which is that prominence plumes are triggered by magnetic Rayleigh–Taylor instability (Berger et al. 2010; Hillier et al. 2012; Xia & Keppens 2016). In other words, the magnetic RT instability is in fact the result of the interaction between an erupting MFR

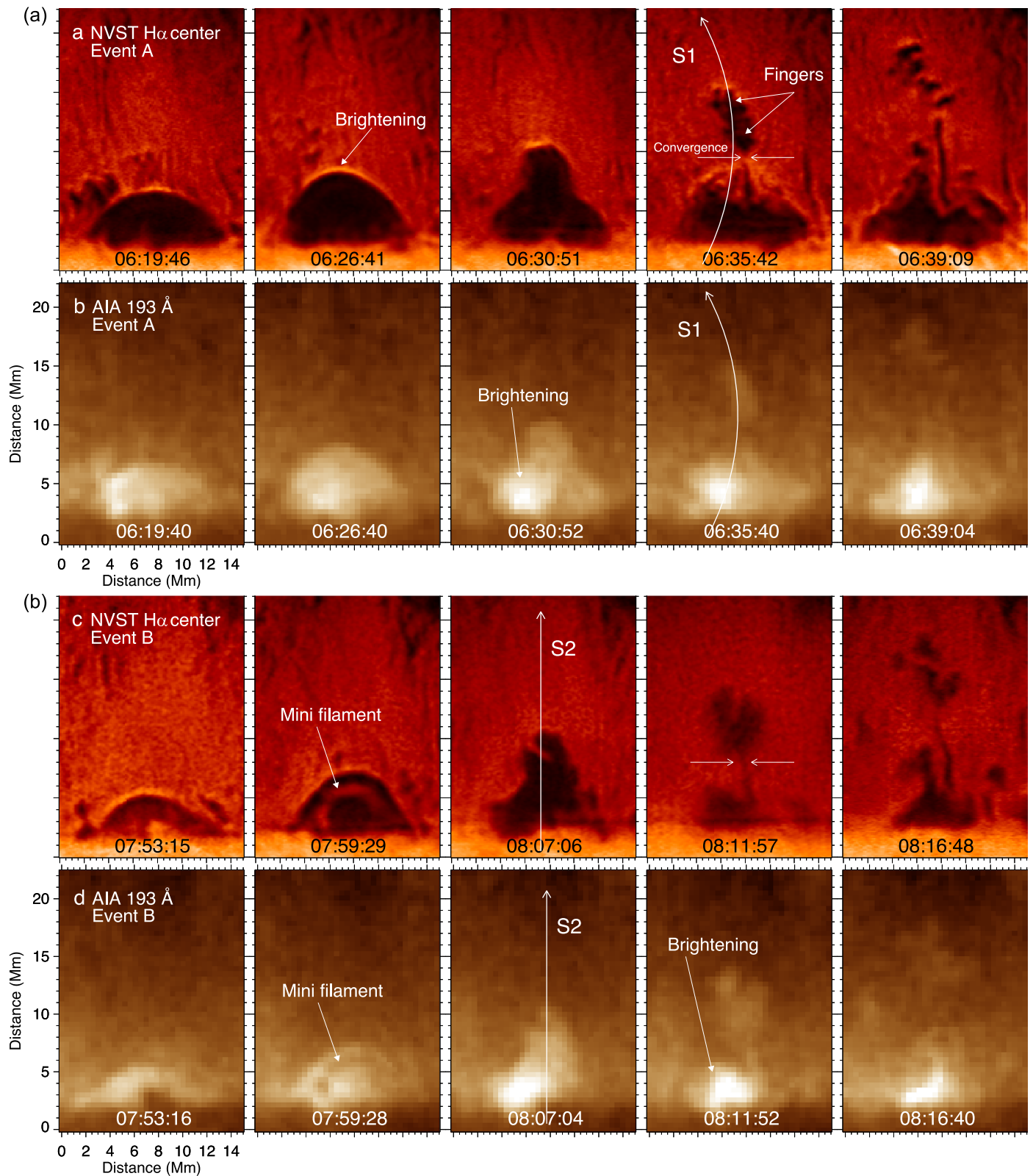


Figure 2. Time series of images during the bubble-plume evolution. (a) NVST $H\alpha$ images of Event A. The brightness enhancement and fingers are noted. Slice S1 roughly tracks the trajectory of the plume A and the time-distance diagram of S1 is plotted in Figure 3. (b) Co-temporal AIA 193-Å channel series of Event A. (c) NVST $H\alpha$ images of Event B. The mini filament inside the bubble is noted. S2 roughly tracks the trajectory of the mini filament and plume B. The corresponding time-distance diagram is plotted in Figure 4. (d) Co-temporal AIA 193-Å channel series of event B. An animation of the two events' evolution is provided. Event A runs from 05:58:59 UT to 07:07:33 UT while Event B begins at 7:23:15 UT and ends at 08:34:48 UT. The real-time duration of the animation is 7 s.

(An animation of this figure is available.)

Animation=mp4,mp4

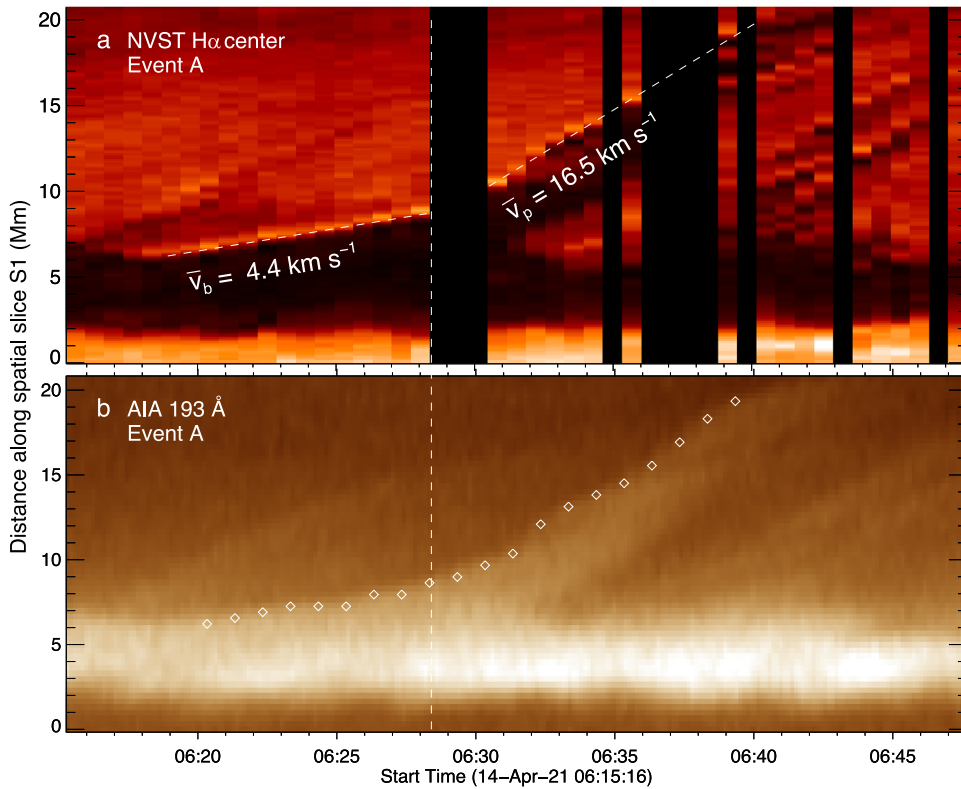


Figure 3. Dynamic evolution of the bubble and plume in Event A. (a) Time–distance diagrams of $H\alpha$ channel along slice S1. The intervals in black are due to the lack of observational data. The bubble–prominence interface shows distinct emission enhancement during its ascent. The vertical dashed line marks the appearance time of the plume. The inclined dashed lines fit the displacements of the bubble and plume and their average velocity is noted by \bar{v}_b and \bar{v}_p , respectively, in this and the following images. (b) Time–distance diagrams in 193 \AA channel. Diamond signs track the displacement of the bubble and plume in detail.

and bubble–prominence interface. Recent high-resolution spectral observation also shows new features at the plume fronts during plume evolution (Xue et al. 2021), like strong blueshifts and turbulence, which are not revealed in the simulations of RT instability. Combined with the fact that RT instability can occur when one fluid penetrates into another, the features mentioned earlier and the fingers due to RT instability are likely caused by the compression of the rising plume on the prominence.

5. Conclusions and Discussions

In both events, there is no obvious perturbation, oscillation, or collapse of the bubble until the plume occurs, which is different from some of the reported events where plumes emerge from a turbulent bubble boundary. Similar characteristics was reported in the plume events observed by the Mauna Loa Solar Observatory (de Toma et al. 2008), including nonturbulent appearance and a bright core embedded inside the bubbles in the bubble formation process, but there was no specific explanation, probably due to limited resolution or viewing angle.

Here, we propose that there is an upward force and/or structure breaking the metastable state where buoyancy is balanced by tension in the magnetic field of prominence, pushing and/or interacting with the top boundary of the bubble to drive the plume, and then fingers form inside the plume due to RT instability. The resulting turbulent boundary allows new plumes to form (Berger et al. 2017). This conjecture is well confirmed in Event B, in which the bubble inflates as the mini filament ascends inside it and the plume occurs shortly after the

mini filament contacts the bubble boundary, suggesting that the eruptive mini filament acts as a driving force for triggering the plume.

What is the story of Event A then? Like many other reported bubble–plume events, no erupting mini filament was observed in EUV and $H\alpha$. Except for this fact, the two events are almost identical. Why? We suspect that there was invisible or faint MFR eruption in Event A. As we already noted, an erupting and expanding MFR is not necessarily filled with enough cold and dense matter to be visible. Eruption and expansion of a mini filament could cause heating inside the MFR or rapid decrease of density, leading to lower brightness in $H\alpha$ images and eventually disappearance of the structure. The rapid disappearance of the mini filament in Event B and many other similar observations (e.g., Panesar et al. 2015) may explain why such an event has rarely been observed.

The similar brightenings in the two events suggest energy release may occur between the MFR and magnetic loops inside the bubble or at the bubble–prominence boundaries. Another possibility is that the brightenings are merely a result of the MFRs sweeping away the cool plasma in the bubbles and revealing the true coronal emissions (Shen et al. 2015; Awasthi & Liu 2019) behind the “curtain.” In either explanation, MFR is the key element here.

Although we emphasize the importance of an emerging magnetic flux rope in the formation of the bubble–plume event, the mechanism of instability at boundaries and reconnection between the erupting MFR and a large filament (e.g., the jet event shown in Shen et al. 2019) cannot be completely discarded. The bubble began to collapse as the plume formed and rose, resulting in the turbulent bubble boundary (Figure 2),

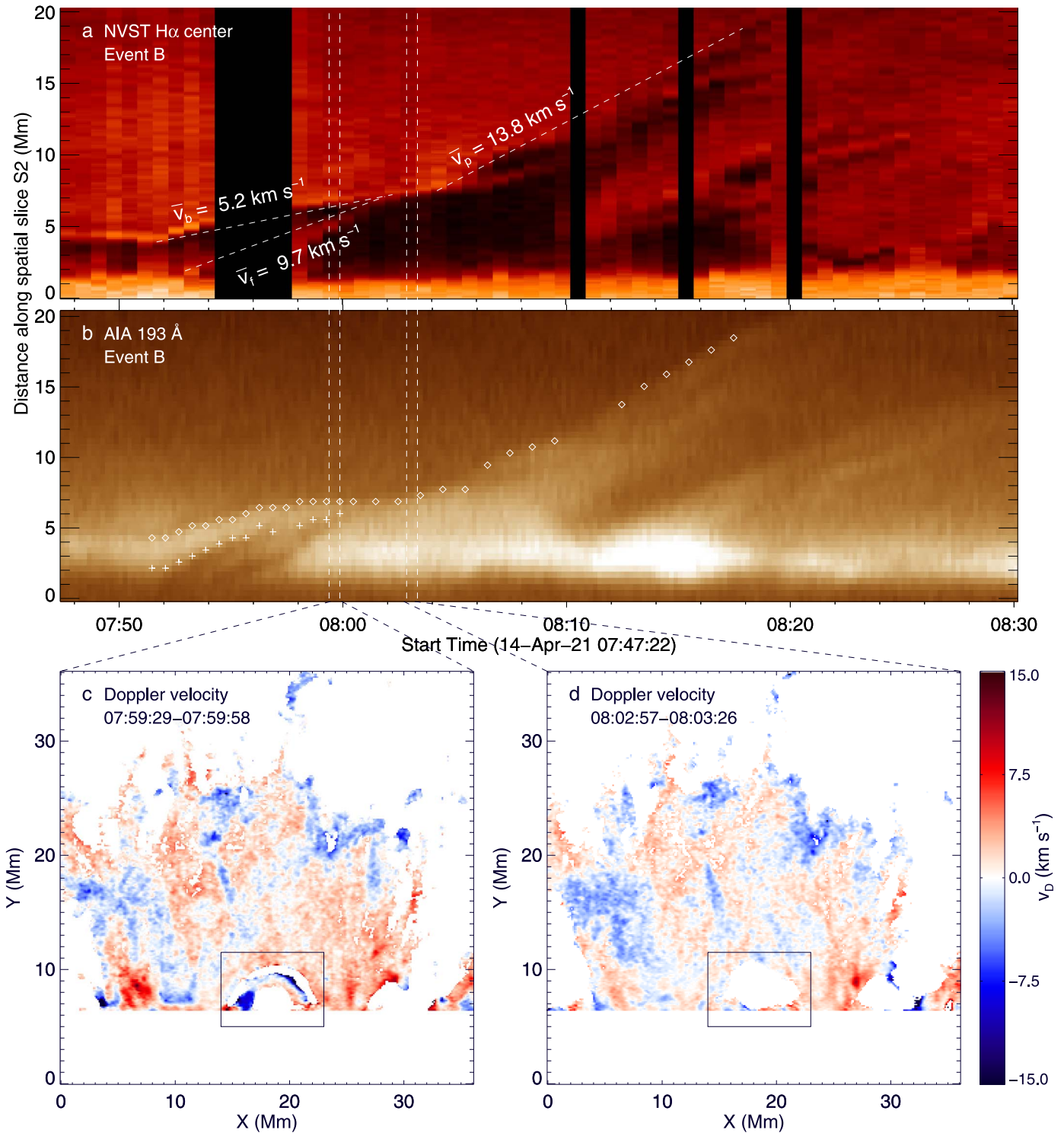


Figure 4. Dynamic evolutions of the prominence bubble and plume in Event B. (a) Time–distance diagram in H α channel along slice S2 in Figure 2. The ascent speeds of the bubble boundary, plume front, and the erupting mini filament are denoted. The Doppler maps shown in panels (c) and (d) are derived from the three-band data observed in the two time ranges indicated by the vertical dashed lines, respectively. (b) The corresponding time–distance diagram in 193 \AA channel. The plus signs track the upper boundary of the erupting mini filament. (c) Doppler map during the eruption of the mini filament. (d) Doppler map after the disappearance of the mini filament. The FOVs of the Doppler maps are marked with the dashed box in Figure 1(d). Note that our calculations of LOS velocities are only applicable for emission H α lines, and the regions <7 Mm are left and shown in white. The black rectangles represent the region of interest. A velocity value of $\sim 1.9 \text{ km s}^{-1}$ due to solar rotation has been subtracted from the Doppler maps.

which is a sign of instability and a source for subsequent plumes. During the penetration of the plume into the prominence, the rapid convergence of the bubble–prominence boundary (Figure 2) from the two sides and the downflows

suggest that reconnection may occur. This process separated the bubble and plume and may help maintain the bubble structure.

To conclude, our observation indicates that bubble–plume events can be caused by eruptive MFR underneath a prominence body. More importantly, eruptive MFR can also transport matter and magnetic flux into prominence from a chromospheric level, which may be conducive to the eruption of a prominence. The question is can other eruptive magnetic structures, such as jets and spicules, also trigger bubble–plume events? More high-resolution observations and MHD simulations are certainly needed.

The $H\alpha$ data used in this paper were obtained with the New Vacuum Solar Telescope in the Fuxian Solar Observatory of Yunnan Astronomical Observatory, CAS. SDO is a mission for NASA’s Living with a Star program. This work is supported by the National Natural Science Foundation of China (grant Nos. 11820101002, 11921003, U1631242, 11427803, U1731241, and U1931138) and the Strategic Pioneer Program on Space Science of CAS (grant Nos. XDA15320300, XDA15016800, XDA15320104, and XDA15052200).

ORCID iDs

Changxue Chen  <https://orcid.org/0000-0002-0562-1282>
 Yang Su  <https://orcid.org/000-0002-4241-9921>
 Jianchao Xue  <https://orcid.org/0000-0003-4829-9067>
 Weiqun Gan  <https://orcid.org/0000-0001-9979-4178>
 Yu Huang  <https://orcid.org/0000-0002-0937-7221>

References

- Awasthi, A. K., & Liu, R. 2019, *FrP*, **7**, 218
 Berger, T., Hillier, A., & Liu, W. 2017, *ApJ*, **850**, 60
 Berger, T., Testa, P., Hillier, A., et al. 2011, *Natur*, **472**, 197
 Berger, T. E., Shine, R. A., Slater, G. L., et al. 2008, *ApJ*, **676**, L89
 Berger, T. E., Slater, G., Hurlburt, N., et al. 2010, *ApJ*, **716**, 1288
 de Toma, G., Casini, R., Burkepille, J. T., & Low, B. C. 2008, *ApJ*, **687**, L123
 Dudík, J., Aulanier, G., Schmieder, B., Zapiór, M., & Heinzel, P. 2012, *ApJ*, **761**, 9
 Feng, S., Deng, L., Shu, G., et al. 2012, IEEE 5th Int. Conf. on Advanced Computational Intelligence, A subpixel registration algorithm for low PSNR images (Piscataway, NJ: IEEE), 626
 Gouttebroze, P., Heinzel, P., & Vial, J. C. 1993, *A&AS*, **99**, 513
 Gunár, S., Schwartz, P., Dudík, J., et al. 2014, *A&A*, **567**, A123
 Guo, Y., Hou, Y., Li, T., & Zhang, J. 2021, *ApJL*, **911**, L9
 Hillier, A., Isobe, H., Shibata, K., & Berger, T. 2011, *ApJL*, **736**, L1
 Hillier, A., Isobe, H., Shibata, K., & Berger, T. 2012, *ApJ*, **756**, 110
 Keppens, R., Xia, C., & Porth, O. 2015, *ApJL*, **806**, L13
 Lawrence, P. 2015, *S&T*, **129**, 77
 Lemen, J. R., Title, A. M., Akin, D. J., et al. 2012, *SoPh*, **275**, 17
 Li, L. P., Peter, H., Chen, F., & Zhang, J. 2014, *A&A*, **570**, A93
 Liu, Z., Xu, J., Gu, B.-Z., et al. 2014, *RAA*, **14**, 705
 Panesar, N. K., Sterling, A. C., Innes, D. E., & Moore, R. L. 2015, *ApJ*, **811**, 5
 Pesnell, W. D., Thompson, B. J., & Chamberlin, P. C. 2012, *SoPh*, **275**, 3
 Shen, Y., Liu, Y., Liu, Y. D., et al. 2015, *ApJL*, **814**, L17
 Shen, Y., Qu, Z., Yuan, D., et al. 2019, *ApJ*, **883**, 104
 Xia, C., & Keppens, R. 2016, *ApJL*, **825**, L29
 Xue, J.-C., Vial, J.-C., Su, Y., et al. 2021, *RAA*, **21**, 222
 Yan, X., Liu, Z., Zhang, J., & Xu, Z. 2020, *ScChE*, **63**, 1656
 Yang, Y.-F., Qu, H.-X., Ji, K.-F., et al. 2015, *RAA*, **15**, 569